Internal stresses in steel plate generated by shape memory alloy inserts

Benoit Malard, Jan Pilch, Petr Sittner, Vadim Davydov, Petr Sedlák, K. Konstantinidis, Darren J. Hughes

Internal stresses in steel plate generated by shape memory alloy inserts

B. Malard [a], J. Pilch [b,c], P. Sittner [b,*], V. Davydov [d], P. Sedlák [e], K. Konstantinidis [f], D.J. Hughes [f,g]

[a] *SIMaP, Domaine Universitaire BP 75, 38402 Saint Martin d'Hères, France*
[b] *Institute of Physics of the ASCR, Na Slovance 2, Praha 18221, Czech Republic*
[c] *Neutron Physics Laboratory, Nuclear Physics Institute, Rez 250 68, Czech Republic*
[d] *Paul Scherrer Institut, ASQ-NUM, 5232 Villigen, Switzerland*
[e] *Institute of Thermomechanics of the ASCR, Dolejškova 5, Praha 18200, Czech Republic*
[f] *Institut Laue Langevin, 6 rue Jules Horowitz, Grenoble 38042, France*
[g] *WMG, University of Warwick, Coventry CV4 7AL, UK*

Abstract

Neutron strain scanning was employed to investigate the internal stress fields in steel plate coupons with embedded prestrained superelastic NiTi shape memory alloy inserts. Strain fields in steel were evaluated at $T = 21$ °C and 130 °C on virgin coupons as well as on mechanically and thermally fatigued coupons. Internal stress fields were evaluated by direct calculation of principal stress components from the experimentally measured lattice strains as well as by employing an inverse finite element modeling approach. It is shown that if the NiTi inserts are embedded into the elastic steel matrix following a carefully designed technological procedure, the internal stress fields vary with temperature in a reproducible and predictable way. It is estimated that this mechanism of internal stress generation can be safely applied in the temperature range from −20 °C to 150 °C and is relatively resistant to thermal and mechanical fatigue. The predictability and fatigue endurance of the mechanism are of essential importance for the development of future smart metal matrix composites or smart structures with embedded shape memory alloy components.

Keywords: Shape memory alloy; NiTi; Residual stress; Neutron diffraction; Strain scanning

1. Introduction

The lifetime of a structural component is usually determined by the interactions between the lattice defects within the component and the stresses to which it is exposed. These stresses are a combination of those applied in service and residual stresses which typically develop during the processing of the component (machining, welding; plastic deformation introduces internal stress while annealing causes stress relief). Whilst the effect of applied stresses can be easily accounted for in the design of a component, it is more difficult when there are unknown residual stresses in it. They are usually unknown because they are difficult to measure reliably and even more difficult to predict [1,2]. If they are not anticipated, residual stresses can add to service loads and result in unexpected failures in a wide range of engineering components. The residual stresses may, however, be also beneficial to the component's performance. For example, surfaces of structural components are subjected to shot peening, which introduces compressive stresses in them, preventing crack nucleation in the surface layer under tensile working conditions [3].

In order to allow for more lightweight design of structural components made of steel as well as to improve their fatigue performance, particularly under thermomechanical loads, we have been investigating the possibility of deliberately introducing internal stresses into structural compo-

* Corresponding author. Tel.: +420 266052657; fax: +420 286890527.
E-mail address: sittner@fzu.cz (P. Sittner).

nents with the help of thermally responsive inclusions (inserts) made of shape memory alloys (SMAs) [4,5]. Since such inserts are considered to be inherent parts of the component, the thermally induced stresses generated in the surrounding material in the absence of external forces are called "internal stresses" – meaning Type-I residual stresses varying within the component over a range much larger than the grain size. Originally, this research was initiated within the collaborative European research project PROSTONE funded by the European Union to modernize Europe's stone industry for "eco-efficient and highly productive stone processing by multifunctional materials" [6]. A range of potential SMA applications in stonecutting equipment has been identified within the project, e.g. thermally activated spacers, vibration control elements, stone splitters, and superelastic elements for cutting chains.

One of the most intensively investigated engineering applications was a "smart cutting disc" – a steel disc for cutting stones reinforced with a suitably located set of superelastic NiTi inserts embedded in prestrained shape into precisely cut holes in the rim of the steel disc (Fig. 1). During cutting, the prestrained NiTi inserts try to expand with increasing temperature [7] and thus generate the desired beneficial internal stresses in selected locations, resulting in two main benefits: (i) elimination of stress concentrations in the disc rim under working conditions allows the design of thinner steel discs; (ii) improved disc design allows for application of more severe cutting conditions (larger pressure and rotating speed), leading to more efficient stone cutting. Additionally the NiTi inserts were found experimentally to improve the vibrational properties of the cutting discs.

Special technology was developed for embedding the prestrained NiTi inserts into steel plates. Smart cutting discs were fabricated and their added functionality was verified by field experiments on marble as well as granite stones [6]. These tests basically confirmed the expected benefits. However, it was not clear whether the selected design was the best one, what the spatial distribution and magnitude of internal stresses around the NiTi insert is, how these stresses change with temperature and external loads, and how many operational cycles the stress generation mechanism will survive. As we gradually started to realize the complexity of the design of adaptive engineering devices with smart SMA inserts, the research program further continued, focusing on basic research around the questions raised above.

Fig. 1. A stone cutting disc with 2 × 16 prestrained NiTi inserts designed by POMDI to alleviate stress concentrations in the rim during working conditions [6].

In this work, part of the research concerning the evaluation of the thermally sensitive internal stress fields around NiTi inserts in steel and functional fatigue of the internal stress generating mechanism is dealt with. Since we were interested in internal stress changes with temperature, all destructive methods were naturally excluded. Probably the best experimental method for such a task is neutron strain scanning [8–11]. We performed conceptual neutron strain scanning experiments on steel plate coupons with a single NiTi insert exposed to varying stress [4] and temperature [5]. The results clearly proved the presence of internal stress distributions around the NiTi inserts varying with the distance from the insert as well as with the temperature and stress. Many unsolved problems, however, still remained. One of them was an uncertainty with the obtained internal stress distribution and another one the possible fatigue of the stress generation mechanisms. Will the NiTi inserts continue to generate desired internal stresses (meaning required stress state, stress level and spatial distribution) after the cutting disc has passed through the large number of thermomechanical cycles expected under working conditions? In order to answer this question we simulated the working conditions by subjecting the steel coupons with NiTi inserts to thermal and mechanical fatigue prior the strain scanning studies. The results are reported and discussed in this paper.

2. Experimental procedures

2.1. Neutron strain scanning method

Since neutrons do not have electric charge, neutron radiation easily penetrates several centimeters through most bulk metals. Neutron strain scanning is already established as an excellent method for nondestructive three-dimensional probing of stresses existing within bulk engineered components [8–11]. In this method, the crystal lattice is used as a built-in sensor capable of detecting minor elastic distortions of the crystal lattice (changes of interplanar spacing) due to the effect of stress (Fig. 2). The stress can be external or internal. If strain scanning is performed at variable temperature, one needs to take into account the fact that lattice spacing varies with temperature due to linear thermal expansion.

When applying the method, the material volume is scanned in the x-, y-, and z-directions with neutron radiation (beam size ~1–2 mm) with a typical spatial resolution of about ~0.1 mm. The neutrons are diffracted by the crystal according to Bragg's equation:

$$n\lambda = 2d\sin\theta \tag{1}$$

where λ is the neutron wavelength, d is the interplanar lattice spacing of the set of lattice planes on which the neutrons are diffracted, and 2θ is the diffraction angle between the incident and diffracted neutron beams. Elastic

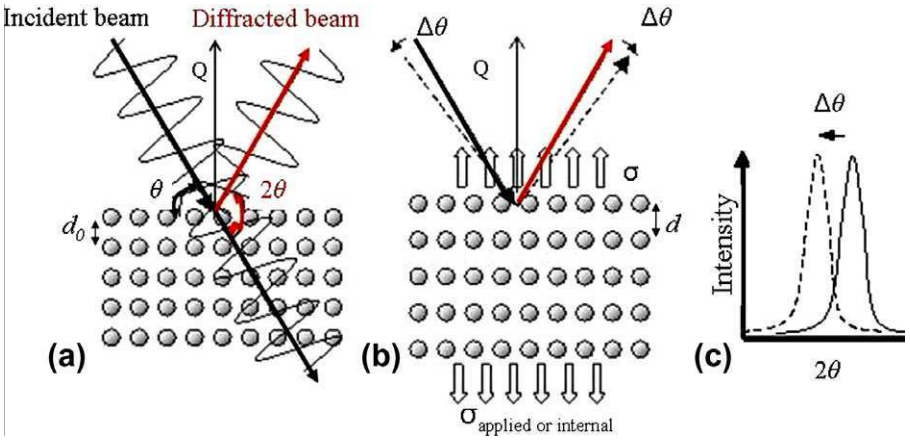

Fig. 2. Principle of the evaluation of elastic strain in crystalline materials by neutron diffraction [8,11]. The incident neutron beam is diffracted under angle 2θ by the set of lattice planes with interplanar spacing d. d_0 is the lattice spacing measured without external stress, $\Delta\theta$ is the change in the Bragg angle caused by the change in the lattice spacing Δd due to the presence of stress in the material. Q is the vector along which each strain component is measured.

strains in the specimen bring about changes in lattice spacing Δd resulting in changes of diffraction angle $\Delta\theta$ evaluated in the experiment as the shift of the associated diffraction peak measured by the detector (Fig. 2). Evaluation of stress in crystalline materials by neutron diffraction thus relies on precise measurements of the small changes of the diffraction angle of a specific purposely selected reflection. The lattice strain and thereafter the stress are evaluated in the following way. Differentiating Eq. (1) and for constant wavelength we obtain:

$$\frac{\Delta d}{d_0} = -\cot\theta_0 \cdot \Delta\theta \tag{2}$$

If we combine Eq. (2) with the definition of strain, $\varepsilon = \frac{\Delta d}{d_0}$,we obtain:

$$\varepsilon = -\cot\theta_0 \cdot \Delta\theta = -(\theta - \theta_0) \cdot \cot\theta_0 \tag{3a}$$

where θ and θ_0 are the Bragg angles for the strained and the unstrained lattice respectively. Strain error $\delta\varepsilon$ related with the precision of the evaluation of Bragg angle θ is calculated by:

$$\delta\varepsilon = -\cot\theta_0 \cdot \delta\theta \tag{3b}$$

Evaluation of the θ_0 (d_0) is discussed further below. Having adequately accurate measurements of the Bragg angle θ in a material point, it is possible to calculate elastic strain from Eq. (3a). If the three principal strains ε_x, ε_y, ε_z in a material point are known, we can calculate principal stress components σ_x, σ_y, σ_z in this point using Hooke's law for isotropic material:

$$\sigma_x = E_h \frac{(1-\nu_h)\varepsilon_x + \nu_h(\varepsilon_y + \varepsilon_z)}{(1-2\nu_h)(1+\nu_h)} \tag{4}$$

where E_h is the diffraction Young's modulus and ν_h is the diffraction Poisson's ratio for a given material and $\{hkl\}$ reflection used in the strain scanning. The other two principal stress components (σ_y, σ_z) are calculated by permuting the x, y, z indices in Eq. (4). The errors in the assessment of stress components σ_i are obtained by differentiating Eq. (4) with respect to all three principal strain components ε_i, since all contribute to the resulting stress tensors. Due to the fact that these errors are statistical and mutually independent, the error of principal stress component $\delta\sigma x$ [12] is written as the quadratic function of the individual strain errors (Eq. (5)). The errors of the other two principal stress components ($\delta\sigma y, \delta\sigma z$) are again calculated permuting x, y, z in Eq. (5):

$$\delta\sigma_x = \frac{E_h}{(1+\nu_h)} \sqrt{\left(1+\frac{\nu_h}{(1-2\nu_h)}\right)^2 (\delta\varepsilon_x)^2 + \left(\frac{\nu_h}{(1-2\nu_h)}\delta\varepsilon_y\right)^2 + \left(\frac{\nu_h}{(1-2\nu_h)}\delta\varepsilon_z\right)^2} \tag{5}$$

If the principal stress directions in isotropic material are known, the strain scanning experiment can be performed as follows. The sample is rotated in such a way that one of the principal stress directions lies parallel to the vector Q corresponding to the selected lattice plane (Fig. 2). The sample is moved with a given scan step with respect to neutron beam in the x-, y-, and z-directions while recording individual diffraction profiles. The internal stress in the material (principal stress components σ_x, σ_y, σ_z) in specific positions) is evaluated from the diffraction data using Eqs. (1), (2), (3a), (3b), (4), (5). The neutron strain scanning method is well developed, particularly for steel as the most important engineering material. Dedicated strain scanning diffractometers exist at most of the large-scale neutron facilities, for example diffractometer SALSA at ILL in France [13], ENGIN-X at ISIS in the UK [14], SMARTS at LANSCE [15], TAKUMI at J-Parc in Japan [16] or VULCAN at SNS in the USA [17].

2.2. Steel coupons with embedded NiTi inserts

Steel coupon samples with prestrained NiTi inserts were prepared for the neutron strain scanning experiments. The

NiTi inserts had a well-defined prism shape, in contrast to elliptical NiTi inserts used in manufacturing smart cutting discs [6] and in earlier strain scanning experiments [4,5]. The steel coupon samples (a kind of NiTi/steel composite unit) were prepared using a procedure described in this section.

2.2.1. Steel coupons

The low alloyed carbon steel disc (350 mm diameter, 2 mm thick; the chemical composition and material parameters are given in Tables 1 and 2) was provided by Spanish company POMDI as a standard material used for the manufacturing of cutting tools in the frame of the research collaboration within the project PROSTONE.

Four prism-shaped steel coupons (30 mm × 30 mm × 2 mm) were laser-cut from the disc. Rectangular holes (7 mm × 3 mm) were cut in the center of the coupons. Laser cutting of both the steel and NiTi prisms was performed at the Research Center of Manufacturing Technology at the Czech Technical University in Prague using research laser Lumonics JK7001H (Nd:YAG crystal; wavelength, 1064 nm; power, max. 550 W).

2.2.2. NiTi inserts

NiTi inserts were laser cut from rolled and flat annealed NiTi plate (80 mm × 25 mm × 2 mm) obtained from Memory Metalle (superelastic alloy S). Transformation temperatures of the alloy were determined by differential scanning calorimetry as $R_s = 8$ °C, $R_f = -22$ °C, $M_s = -48$ °C and $M_f = -110$ °C, $A_s = -9$ °C, $A_f = 26$ °C. 20 pieces of prism-shaped specimens with dimensions 3.0 mm × 7.2 mm × 2.1 mm were cut with the long edge aligned with the rolling direction. While embedding the inserts into the holes within the steel disc they will be deformed in compression at very low temperature, which is not harmful for the shape memory alloy material since deformation up to ~5% takes place at relatively low stresses. During the stone cutting operation, however, the NiTi inserts in the rim (Fig. 1) will be heated from the room temperature up to 130 °C. This will induce large compressive stress in them and, moreover, they will be periodically loaded in compression as the rotating disc is pushed towards the stone during the cutting. The NiTi inclusions are thus expected to be exposed to periodical variation of stress of the order of hundreds of MPa at rather high temperatures for superelastic Ni-rich NiTi alloy [18]. It is well known that bulk NiTi is not resistant to plastic deformation, particularly at temperatures above 100 °C. We were concerned that the inserts might be plastically deformed due to the combination of overheating/overloading, which may decrease the compressive prestrain and affect its capability to generate stress upon constrained heating. Hence, we decided to "train the NiTi inserts" by compression cycling at room temperature prior to embedding them into steel to avoid the potential danger of the later failure of the stress generation mechanism.

Table 1
Chemical composition (wt.%) of the low alloy carbon steel 75Cr1.

C	Si	Mn	P	S	Al	Cr
0.764%	0.320%	0.740%	0.015%	0.002%	0.007%	0.340%

Table 2
Mechanical properties of the low alloy carbon steel 75Cr1.

Tensile strength	Yield stress	Young's modulus	Poison ratio
980 MPa	780 MPa	229 GPa	0.3

Prismatic NiTi specimens were subjected to compressive mechanical cyclic loading in a servohydraulic testing machine INSTRON 8872. The shape of the superelastic stress–strain curve (Fig. 3a) evolves significantly during cycling, the transformation part becomes steep, hysteresis width decreases and irreversible plastic deformation reaches 1.2% after 5000 cycles (Fig. 3b). The superelastic stress–strain response varies most dramatically in the first 20 cycles and becomes almost stable beyond 3000 cycles. The ability of the trained NiTi element to develop repetitively sufficient force upon constrained heating was also investigated. The trained NiTi insert was loaded up to 1.6% of compressive deformation at room temperature, constrained under a stress of 300 MPa and heated repeatedly to 130 °C under constant length. It was confirmed that the thermally cycled trained NiTi insert was capable of developing ~700 MPa compression stress at high temperature in a stable repetitive manner; the stress generation capability, however, deteriorates with cycling. Based on the results of these studies, it was decided to perform 10–20 compression training cycles

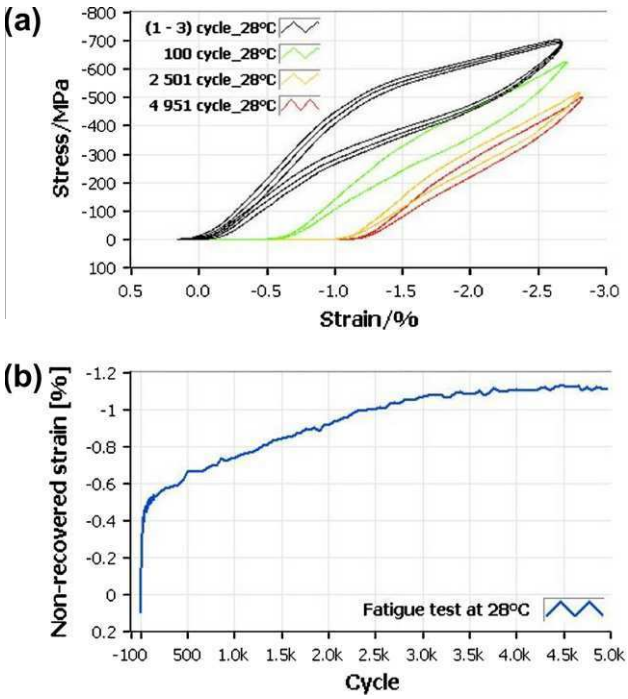

Fig. 3. Training of the NiTi insert in compression (3.0 mm × 7.2 mm × 2.1 mm, 5000 cycles at room temperature, strain rate 0.28 s^{-1}, strain amplitude 2.7%): (a) cyclic pseudoelastic stress–strain curves at room temperature, (b) evolution of nonrecoverable plastic strain during cycling.

for optimizing the thermomechanical response of the NiTi insert for the stress generation functionality and stability.

2.2.3. Procedure for fabrication of steel coupons with NiTi inserts

It is essential to realize that the NiTi inserts can respond to temperature variations by generating stresses in their surroundings only if they are properly embedded in a partially deformed state [7]. Consequently, the technology employed for embedding the inserts into the steel is what actually makes the steel coupon with embedded NiTi insert become a unit of "smart" metal matrix composite. This is why the sample preparation technology is very important and extensively dealt with in this section.

The following procedure was used to fabricate the steel coupon samples for neutron strain scanning experiments. NiTi prisms 7.2 mm × 2.9 mm × 2.1 mm cut from the NiTi plate with longer edge parallel to the rolling direction were polished so that the opposite faces were exactly flat and parallel. The prisms were mechanically trained in cyclic compression at room temperature (S2: 20 cycles, S3: 10 cycles). The dimensions of the trained prisms were 7.12 mm × 2.92 mm × 2.01 mm. The trained NiTi prisms were embedded into the steel coupons (Fig. 4a) using the following procedure. The NiTi insert was cooled by liquid nitrogen vapor to the martensite state ($M_f = -110$ °C), where it can be relatively easily deformed up to 6% and stays in the deformed martensite shape as long as the temperature does not rise above the austenite start temperature ($A_s = -9$ °C). Hence, the deformed NiTi insert could be freely inserted at low temperature (~−50 °C) into the hole. As the temperature increased above the A_s temperature, the insert expanded against the steel in the x-line and developed compressive stress corresponding to a compressive strain of 1.7% (prestrain $(l - l_0)/l_0 = (7.12 - 7)/7 = 0.017$). Note that the NiTi insert never comes into contact with the y-faces of the hole.

As pointed out in the Introduction, besides mapping the internal stress field in the surrounding steel, the goal of this work was also to find out whether the proposed functionality of the insert (generation of desired thermally sensitive internal stress field in the steel plate) is fatigue resistant – i.e. whether the NiTi inserts will generate significant internal stresses in the steel even after it has been exposed to cyclic variation of external mechanical and thermal loads. To simulate these conditions, the steel coupon samples S2 and S3 (Table 3) were also subjected to mechanical fatigue (20,000 compression cycles at 100 °C between 2200 N and 22,000 N (corresponds to 367 MPa in steel) along the x-line) and thermal fatigue (200 thermal cycles between 21 °C and 100 °C), respectively.

2.3. Neutron strain scanning experiments

The strain scanning experiments were performed on the high-resolution two-axis neutron stress/strain diffractometer SALSA at ILL [13]. The diffractometer uses a six-axis robotic Stewart platform (hexapod) to mount, move and rotate the sample with respect to the neutron beam. It combines high load-carrying capacity and large limits of translation with excellent positioning accuracy (±50 μm). SALSA is dedicated to the determination of residual stresses already existing in components of "real" engineering structures. The high-flux neutron beam at ILL enables residual stress measurement deep within bulk engineering materials (aluminum, nickel, steel, titanium, etc.). The beam coming out of the neutron guide is deflected off the Si crystal monochromator, which is adjustable, to define the wavelength of the incident beam. The wavelength of thermal neutrons used in the experiment was $\lambda = 1.5488$ Å. The sample was mounted on the hexapod in a vertical position (Fig. 4b). A purpose-made optical fur-

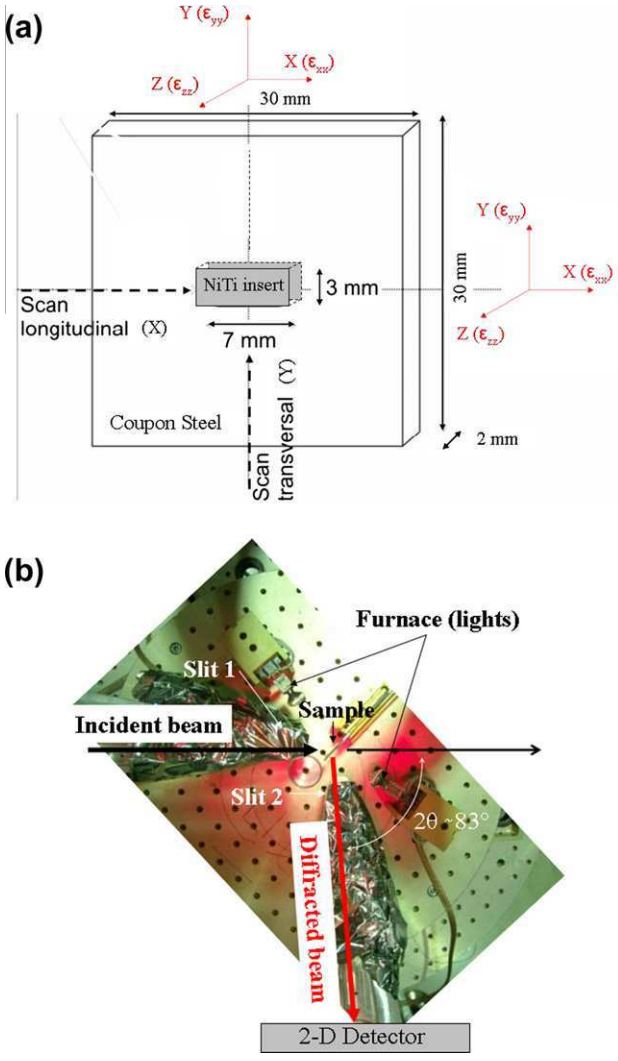

Fig. 4. Neutron strain scanning experiment: (a) schematic sketch of the steel coupon sample with NiTi insert showing two coordinate systems (origins in the middle of the plate at the NiTi–steel interface) used in longitudinal scan along the x-line and transversal scan along the y-line; (b) a top-down view of the steel coupon mounted in vertical position on the specimen stage of the SALSA hexapod platform. The coupon was heated by two halogen lamps. The slits 1 and 2 guiding the incident and diffracted beams were protected against the heat with aluminum foils.

nace consisting of two halogen lamps, a thermocouple attached to the steel and LabView controller was installed on the hexapod to keep the sample at $T = 130$ °C during the measurement.

The slits (1 and 2) adjusting the width of the incoming and diffracted beam (Fig. 4b), respectively, define the gauge volume in the sample where the diffraction information on lattice strain comes from. As the lattice strains were considered to vary significantly in space, it was required to use the smallest gauge volume possible. On the other hand, we needed a gauge volume large enough to achieve sufficient neutron counts within reasonable time. Therefore, the dimensions of incident and outgoing slits were compromised as 1 mm wide and 1 mm high. This resulted in a sample gauge volume of $\sim 1.6 \times 1.6 \times 1.6$ mm^3 due to beam divergence. Neutron detection was achieved by a two-dimensional microstrip detector with an active area of 80 mm × 80 mm. The $\{2\,1\,1\}$ reflection ($2\theta_0 = 83.19259° \sim d_0 = 1.1665$ Å) from the diffraction pattern of the steel was selected for the strain scanning experiments. For the NiTi inclusion to be invisible for neutron diffraction, it is essential that no reflection of the austenite phase of the NiTi appears at this diffraction angle [19]. Although there is a $\{2\,2\,0\}_{\mathrm{m}}$ reflection of the compression stress induced monoclinic B19' martensite phase at lattice spacing 1.176 Å, its intensity and volume fraction of the martensite in prestrained NiTi are too low to affect the strain scanning data recorded at the NiTi/steel interface. The collected diffraction patterns were processed (peaks fitted with a Gaussian profile function to obtain peak position) using the Large Array Manipulation Program (LAMP) used for the data treatment at ILL.

2.4. From diffraction patterns to internal stress field

As introduced in Section 2.1, internal stress field evaluation by the neutron strain scanning method basically involves calculation of spatially resolved stresses from elastic strains obtained from positions of the diffraction peaks recorded in defined material points. Using the SALSA strain scanner, only one component of the strain tensor can be obtained from a single neutron diffraction measurement in a material point. If we know the directions of principal stress components in the isotropic material, three measurements in three principal stress directions are sufficient to evaluate the principal strain ($\varepsilon_x, \varepsilon_y, \varepsilon_z$) and principal stress ($\sigma_x, \sigma_y, \sigma_z$) components in the material point. Considering the symmetry of the internal stress field (expanding NiTi insert pushes in the x-direction while no contact exists between the insert and steel in the y-direction) and measurement geometry (measurement points lie along the x- and y-lines and strain measurements are performed in x-, y-, and z-directions), we see that this is exactly the case in the present experiment (Fig. 4). Principal strain components are denoted according to the coordinate systems in Fig. 4a. Strain scanning experiments were performed by measuring the $\{2\,1\,1\}$ lattice plane spacing in three directions along the x-line (longitudinal scan) and y-line (transverse scan). Lattice strain and its error (corresponding to precision with which the peak position are evaluated) were calculated in $[x, y]$ measurement points from the lattice spacing using Eqs. (2) and (3). The zero positions in each strain scan were set as suggested in Fig. 5 and a scan step of 0.25 mm was used. Individual strain scanning experiments along both x- and y-lines (denoted as Exps. 1–8 in Table 3) were largely automated.

The strain scanning experiments were performed on virgin coupons S2 and S3 at room temperature $T = 21$ °C (Exps. 2 and 6) and at high temperature $T = 130$ °C (Exps. 3 and 7). In order to find out whether the NiTi inserts will generate significant internal stresses in the steel even after it has been exposed to cyclic variation of mechanical and thermal loads expected to occur during service, we evaluated the internal stress distributions from the results of strain scanning experiments performed also on steel coupon samples subjected to mechanical (Exps. 4 and 5) and thermal (Exp. 8) fatigue. To prevent a possible damage of NiTi insert due to overheating, the room temperature experiments (Exps. 1, 2, 6) were performed first, followed by the high temperature experiments (Exps. 3 and 7) and experiments on fatigued samples (Exps. 4, 5, 8). Results of each neutron strain scan can be presented in the form of a diagram showing spatial distribution of three principal strain components ε_x, ε_y, ε_z. The internal stress tensor in a material point was evaluated from the measured lattice strains either directly using Eqs. (1), (2), (3a), (3b), (4), (5) (Section 2.1) or through strain-fitted inverse finite element (FE) simulation (Section 3.3).

The key issue is the error associated with the stress evaluation. In addition to the basic experimental error given by

Table 3
List of strain scanning experiments.

EXP.	Sample	Temperature (°C)	Sample history
EXP1	S1	21	Reference sample without the NiTi insert
EXP2	S2	21	Virgin sample
EXP3	S2	130	Virgin sample
EXP4	S2	21	20,000 compression cycles at 100 °C between 2200 N and 22,000 N along x-direction
EXP5	S2	130	20,000 compression cycles at 100 °C between 2200 N and 22,000 N along x-direction
EXP6	S3	21	Virgin sample
EXP7	S3	130	Virgin sample
EXP8	S3	130	200 thermal cycles 21–100 °C

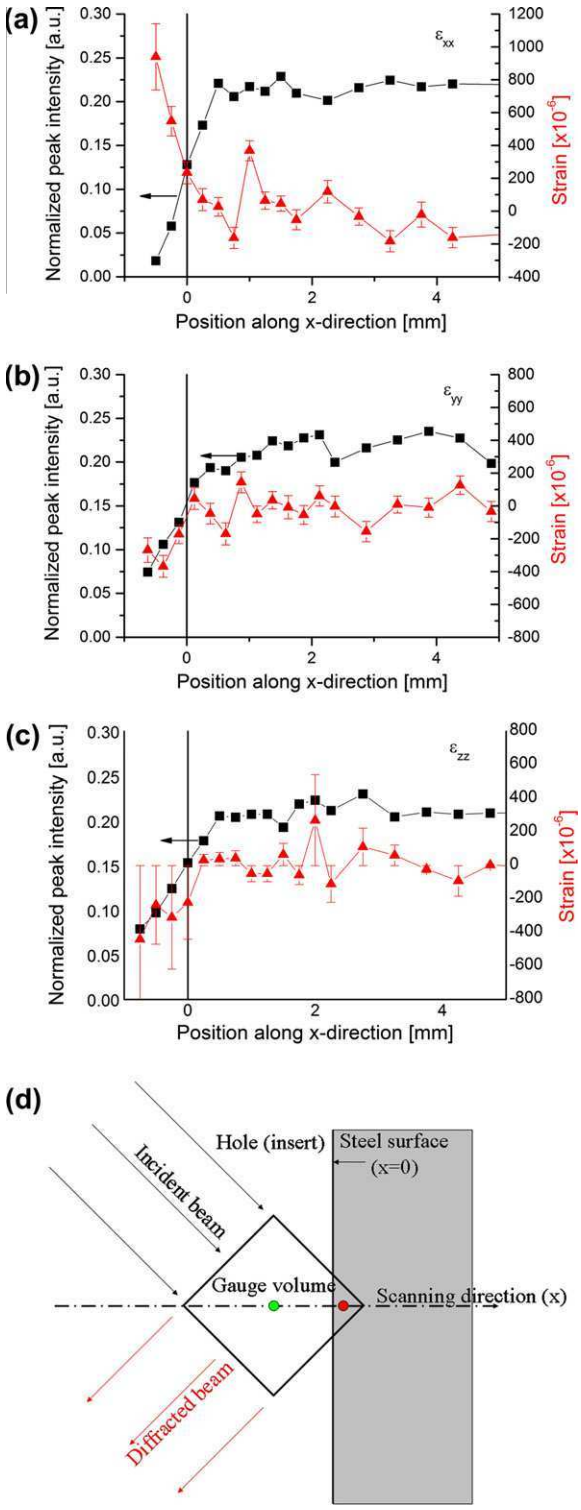

Fig. 5. Setting the zero position in the neutron scans along the x-line using reference sample S1. The $x = 0$ position points in each scan were set so that the nominal center of gravity of the gauge volume (green circle in (d)) coincides with the edge of the hole by assuming that the peak intensity (a–c) should be at the half of the intensity in saturation from symmetry reasons. (d) The sketch of the gauge volume crossing the edge of the hole (surface) during the scan. Provided the surface of the hole was not affected by the laser cutting, the "lattice strains" ε_{xx}, ε_{yy}, ε_{zz} at negative positions are pseudo-strains purely due to the surface effect. (For interpretation of the references to colour in this figure legend, the reader is referred to the web version of this article.)

the precision by which the peak position can be evaluated with the used instrument (given by error bars in Figs. 5–12), the stress results can be significantly affected by multiple supplemental experimental errors made while processing the raw diffraction data. This means that, although the spatially resolved relative variation of lattice spacing is measured relatively precisely by the neutron diffraction, the actual error in the evaluation of internal stress may be significantly larger. Since these supplemental errors are not covered by the error bars in Figs. 8–12, it is of interest to look at the individual steps of the evaluation procedure where these supplemental errors are most likely to be introduced.

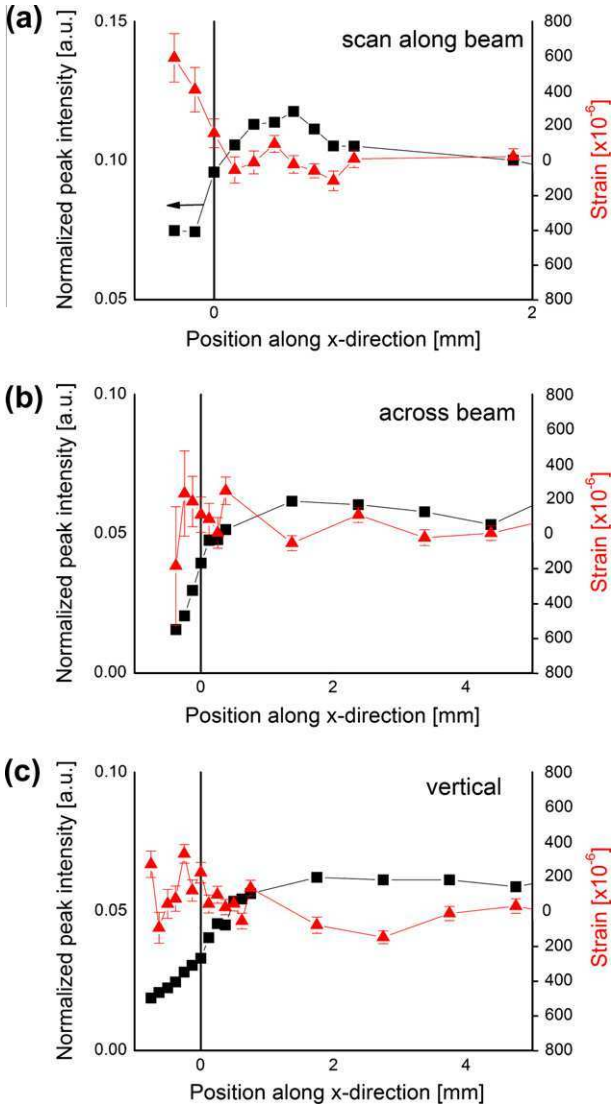

Fig. 6. Evaluation of the pseudo-strains due to the surface effect using steel powder in a container. Lattice strains and intensity of {211} reflection were evaluated by scanning the powder along (a) across (b) and vertical (c) towards the incoming neutron beam (see the experiment geometry in Fig. 4). Zero position is set to the edge of the container similarly, as introduced in Fig. 5d. The surface effect is important mainly while scanning along the beam and only when less than half of the gauge volume is immersed.

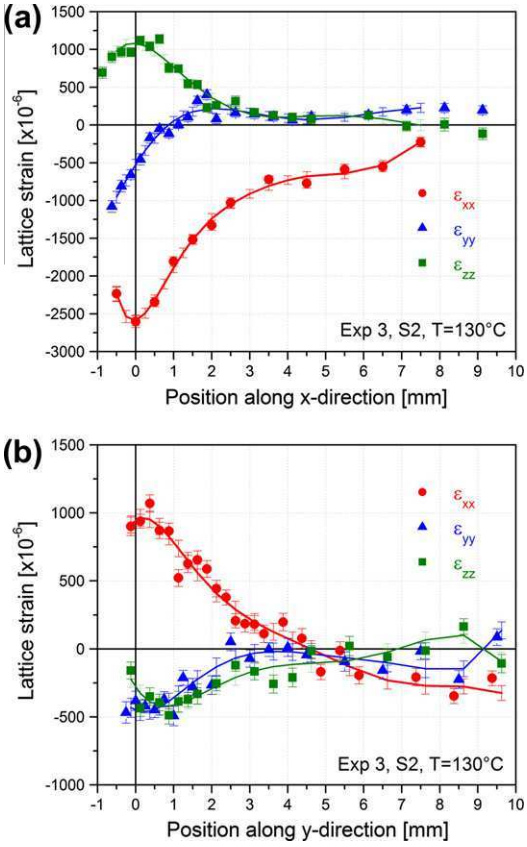

Fig. 7. Lattice strain components ε_{xx}, ε_{yy}, ε_{zz}, measured on virgin sample S2 at temperature $T = 130$ °C in longitudinal scan along the x-line (a) and transverse scan along the y-line (b).

2.4.1. Selection of the shape and size of the gauge volume and scan step

It is essential to note that the stresses and strains obtained from the diffraction measurements are always obtained as average values over the gauge volume of specific size and shape. If the internal stress varies significantly over the length scale less than the relatively large gauge volume (>1 mm^3) typically used in neutron strain scanning experiments (if there is second-order space derivative of strain considerably different from zero), the diffraction averaging with respect to the center of the gauge volume becomes a source of a supplemental error in stress evaluation which is very difficult to estimate. This is in fact frequently the case when strain scanning is performed near sharp corners, inclusions and interfaces in materials.

2.4.2. Selection of the {hkl} reflection

Strain scanning must be made on crystallographic planes which produce an intense diffraction peak at an angle 2θ close to 90° (Fig. 2) so that an approximately square cross-section sampling volume (Fig. 4) is produced. It is also important that the reflection shifts linearly with increasing applied stress and represents bulk elastic behavior of the material as close as possible [20]. If this is not true, significant error can be introduced into the stress

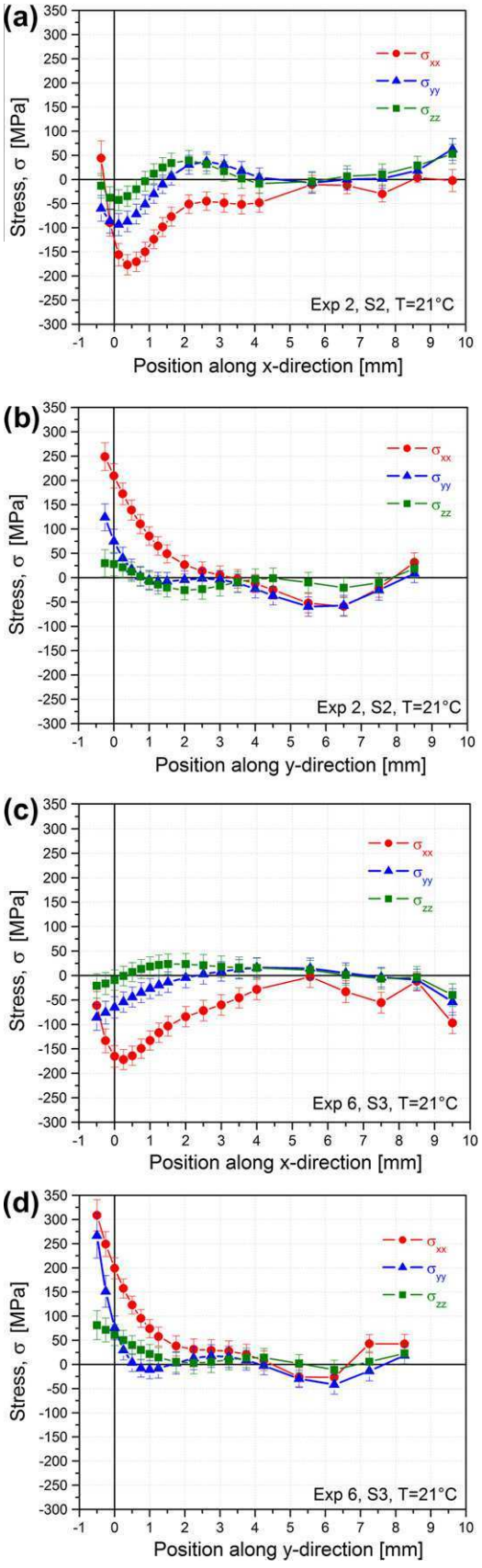

Fig. 8. Internal stress in virgin samples S2 and S3 at $T = 21$ °C – stress components σ_{xx}, σ_{yy}, σ_{zz} evaluated from the strain scans along the x-line (a and c) and y-line (b and d).

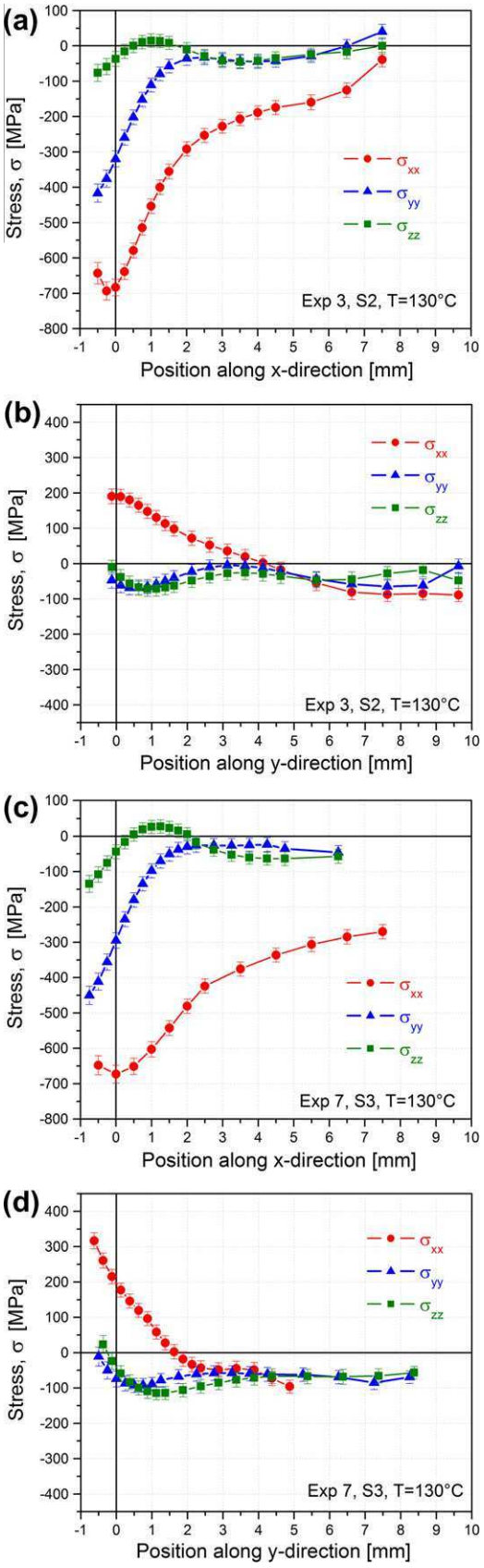

Fig. 9. Internal stress in virgin samples S2 and S3 at $T = 130$ °C – stress components σ_{xx}, σ_{yy}, σ_{zz} evaluated from the strain scans along the x-line (a and c) and y-line (b and d).

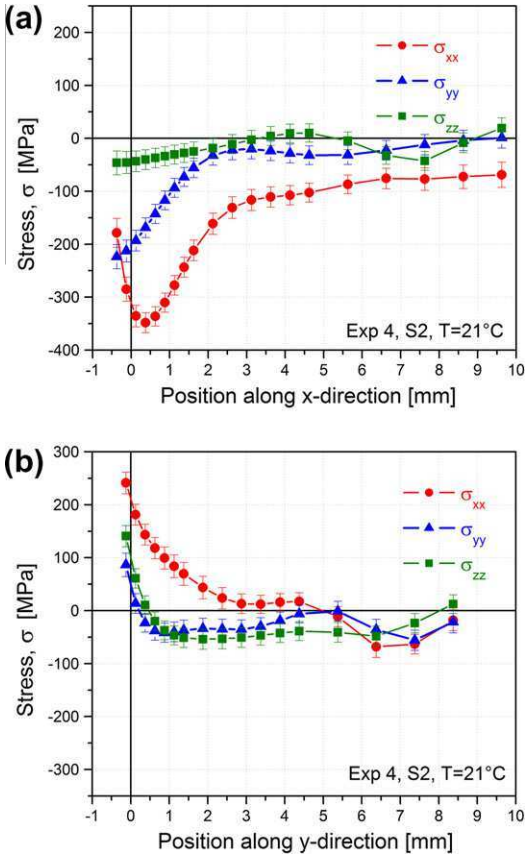

Fig. 10. Internal stress in mechanically fatigued sample S2 at $T = 21$ °C – stress components σ_{xx}, σ_{yy}, σ_{zz} evaluated from the strain scans along the x-line (a) and y-line (b).

calculation, particularly at stresses approaching the yield limit of the studied material.

2.4.3. Coordinate transformation

The hexapod translator's coordinates need to be converted into sample-based coordinates (Fig. 4a). This was done by setting the zero position to coincide with the edge of the hole along each scan line (x, y) by calculating the mid-point of increase of the normalized diffraction peak intensity vs. translator position plot (Fig. 5a–c). Due to the symmetry, half of the gauge volume is thus immersed in the sample (Fig. 5) at the zero position measurement. Any error in zero setting (e.g. mutual shift in position between ε_x, ε_y, ε_z datasets) would adversely affect the stress values calculated using Eq. (4).

2.4.4. The stress-free lattice parameter d_0,

This parameter, which is necessary for calculation of lattice strains (Eqs. (3)), was measured on reference sample S1 (stress-free steel without the NiTi insert) at room temperature $T = 21$ °C as $d_{0,211} = 1.1665$ Å. In fact potential residual stresses in the rolled steel plate causes the {2 1 1} lattice spacing to be slightly different when measured along the x- and y-lines. Neglecting this difference introduces error into the stress evaluation.

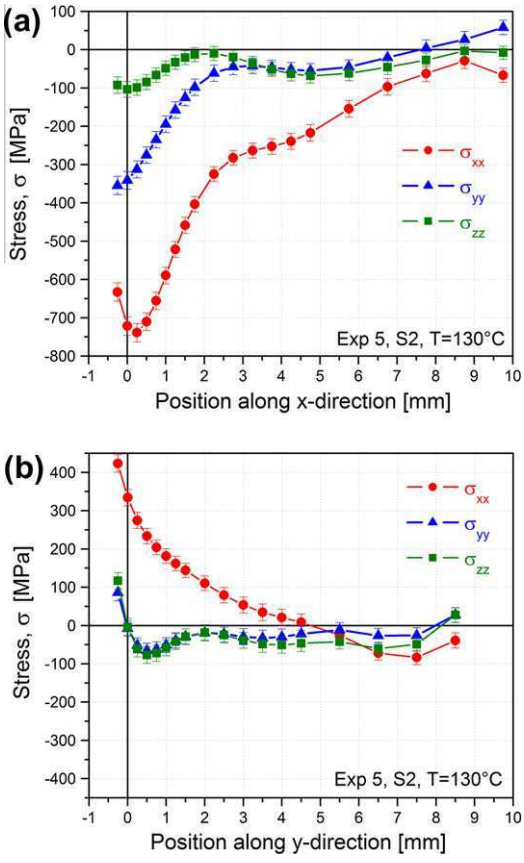

Fig. 11. Internal stress in mechanically fatigued sample S2 at $T = 130$ °C – stress components σ_{xx}, σ_{yy}, σ_{zz} evaluated strain scans along the x-line (a) and y-line (b).

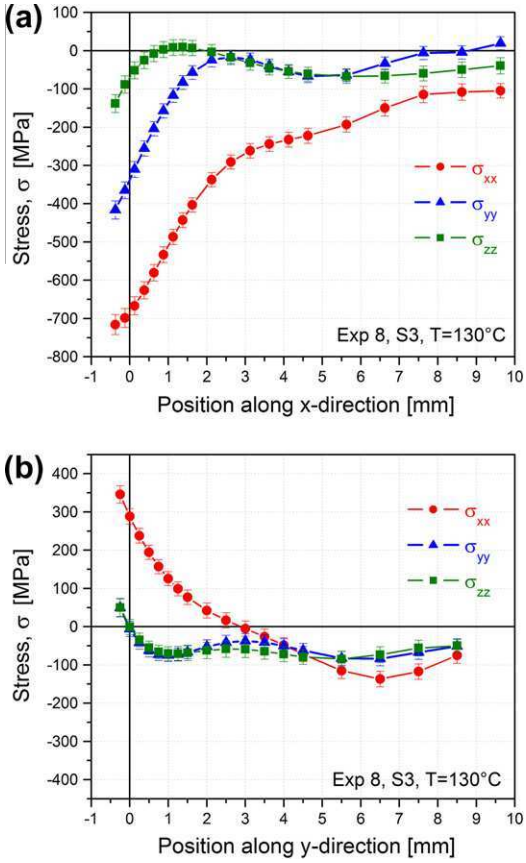

Fig. 12. Internal stress state in thermally cycled samples S3 at $T = 130$ °C – stress components σ_{xx}, σ_{yy}, σ_{zz} evaluated from the strain scans along the x-line (a) and y-line (b).

2.4.5. Subtraction of thermal expansion

The lattice strains due to thermal expansion must be subtracted in order to receive true lattice strains due to stress. The influence of thermal expansion was determined by performing a supplementary diffraction measurement of lattice expansion due to thermal change only using the reference steel sample S1. The obtained result ($d_0 = d_0(T)$) corresponds very well to the value of the linear thermal expansion coefficient (CTE) for ferritic steel, $\alpha = \sim 1.178 \times 10^{-5}\,\mathrm{K}^{-1}$, [21] as well as to the CTE ($1.18 \times 10^{-5}\,\mathrm{K}^{-1}$) obtained in our earlier experiments [4,5]. The lattice strains reported in Sections 3.1 and 3.3 were calculated using d_0 values appropriate for each given temperature, which is equivalent to the subtraction of thermal expansion.

2.4.6. Surface effect

There is an artificial surface effect on the measured strains due to pseudo-peak shifts introduced by the experimental set-up which have their origin in a geometric displacement of the center of gravity of the intensity distribution in the sampled gauge volume combined with the wavelength distribution present in the primary beam [22]. The gauge volume is not fully immersed in the material in measurements performed near the surface. There is hence a small shift in measured positions of diffraction angle because of the difference between nominal and actual wavelengths in the beam. This effect should be compensated where appropriate to give the real lattice strain and therefore real stresses. A correction for the actual position of the gauge volume near the surface was originally considered as follows. When the gauge volume is only partially immersed in the sample there is a difference between the center of gravity of the nominal and the actual gauge volume, respectively (Fig. 5d). The measurement points with values near zero (± half the gauge volume diagonal) should thus be corrected in position so that they correspond to the respective positions of the center of gravity of the actual gauge volume. In order to determine the correction for strains due to the surface effect we have measured a steel powder sample in a container (stress-free state guaranteed) along three orthogonal directions: along the beam, across the beam, and vertical to the beam (simulating measurements along the x-, y-, and z-directions) (Fig. 4). Using Eqs. (3) we calculated the pseudo-strain due to the surface effect and its error. The results shown in Fig. 6 suggest that the surface effect is largest in the case of scans along the beam and that we can ignore the surface effect in measurements where more than half of the gauge volume is immersed in the sample (positive position values). This is

additionally confirmed by the measurements on reference sample S1 (Fig. 5), showing that the strain values in positive position points are, with the exception of the ε_{xx}, minimally affected by the surface effect. Since the internal stresses right at the hole edge were not of critical importance, we decided at that time (experiment was carried out in 2008) not to make the detailed corrections but simply neglect the measurements in negative points in the stress analysis. At present, an analytical mathematical model [22] can be used to correct the results of strain scanning measurements at SALSA for pseudo-peak shifts and determine the measuring positions. The internal stresses can thus be reliably determined as close as 0.04 mm from a surface or interface if needed.

2.4.7. Stress gradient effect at the surface

At the edge of the hole (surface) where largest stress gradients exist, the diffracting volume becomes significantly smaller (Fig. 5d) than 1.6 mm × 1.6 mm × 2 mm in the bulk. The lattice strains measured in points approaching the edges (scan positions near 0) would be adversely affected due to the diffraction averaging over a gauge volume of variable size.

2.4.8. Diffraction elastic constants E_h, ν_h

In order to evaluate stress from lattice strain using Eq. (4) (Section 2.1) as well as using finite element simulations of lattice strains (Section 3.3), diffraction elastic constants E_h, ν_h for the used {2 1 1} reflection of the steel need to be known. The values $E_{211} = 216$ GPa, $\nu_{211} = 0.27$ used in the stress calculation were taken from Ref. [20].

2.4.9. Lattice strain interpolation

After transformation from instrument coordinates to sample coordinates the strain measurements are not in exactly the same x,y position points. In order to calculate stresses, the scattered values of the experimentally measured lattice strains (Fig. 7) were first interpolated and these interpolated strain values (and interpolated strain errors) were used for determining of all three stress components and stress errors in each interpolated position point using Eqs. (4) and (5). This interpolation is a possible source of additional error, which was not taken into account.

2.4.10. Assumption on principal strain and stress

Eqs. (2)–(5) can used to evaluate stress in a material point only if we are sure that the x-, y- and z-axes are principal stress axes of the stress state in that point. With no assumptions as to the strain state, strain measurements have to be performed in at least six directions and the general continuum elasticity scheme needs to be applied to obtain the full stress tensor in a material point [8]. If the assumption on principal strain state is not correct, significant error is introduced into the direct calculation of stress which is very difficult to estimate.

3. Experimental results

3.1. Lattice strains

Spatial distribution of lattice strains (three principal strain components ε_{xx}, ε_{yy}, ε_{zz} calculated using Eq. (3a) and corresponding error using Eq. (3b) measured along x- and y-lines (Fig. 4a) represents "raw experimental data". These were then used to calculate spatial distribution of principal stress tensor components (three principal stress components σ_{xx}, σ_{yy}, σ_{zz}) in samples S2 and S3 at two different temperatures and two different thermomechanical histories (Table 3). The sample S1 is a reference sample without the insert; samples S2 and S3 differ only by the number of mechanical training cycles given to the NiTi insert. Since only stress results are presented and discussed in Section 3.2, let us briefly discuss, as an example, the raw experimental data using the strain scanning results obtained from virgin sample S2 at $T = 130$ °C presented in Fig. 7. Additional strain data are presented in Fig. 14.

The three measured lattice strain components vary along the x-line (Fig. 7a) as well as along the y-line (Fig. 7b) as expected since heating the sample to 130 °C makes the compressed NiTi insert generate internal stresses in the surrounding steel with the maxima at the edges. One can clearly see that particularly the ε_{xx} component varies significantly both along the x-line (compressive) and y-line (tensile). The strain gradients extend up to ~7 mm from the insert edges. The results measured on slightly different samples S2 and S3 (differing in adopted mechanical and thermal training of NiTi inserts) are rather similar (Fig. 14). Concerning the measurement along the y-line, we shall be reminded that the insert never comes into contact with the steel. Lattice strains measured at negative x- and y-coordinates are significantly affected by the surface effect and are unreliable (gauge volume <50% of bulk gauge volume). The strain values in negative positions shown in Fig. 7 are used to calculate the stresses in Section 3.2 but not in Section 3.3.

3.2. Internal stresses calculated directly from the measured strains

The obtained three principal strain components ε_{xx}, ε_{yy}, ε_{zz} were converted into internal stress components σ_{xx}, σ_{yy}, σ_{zz} of the principal stress tensor using the conventional direct approach presented in Section 2.1. When calculating the stress components, the scattered values of the experimentally measured lattice strain were first interpolated (see Fig. 7) and these interpolated strain values (and interpolated strain errors) were used to calculate three stress components in each interpolated position point using Eq. (4). Variations of internal stress along the x- and y-lines (three principal stress components) calculated from lattice strains measured in Exps. 2–8 (Table 3) are presented in Section 3.2 (direct approach) and those determined by

FE modeling are presented in Section 3.3 (inverse approach). Since no compensation of surface effect for position and strain was adopted, the stress values at negative positions (Section 2.4, Fig. 5) are strongly affected by the surface effect. They are shown in Figs. 5–12 just to document what was written about the surface effect.

3.2.1. Internal stress in virgin coupons

Results of the measurements performed on virgin samples S2 (Exp. 2) and S3 (Exp. 3) at room temperature (Fig. 8) show that significant internal stresses already exist in the steel coupon at room temperature. The out-of-plane stress component σ_{zz} is near-zero as would be expected (which is a good indicator that the chosen reference value is valid) and will be neglected in further discussion. There is a bi-axial compressive stress (stress components σ_{xx} and σ_{yy} varying along the x-line maximum $[-175\ \text{MPa}, -88\ \text{MPa}]$) and a bi-axial tensile stress – varying along the y-line maximum $[212\ \text{MPa}, 76\ \text{MPa}]$). The stress maxima appear at the edges and the stress field extends up to 5 and 3 mm from the edge along the x- and y-lines, respectively. This internal stress was established when the compressed NiTi insert expanded against the steel hole when the temperature increased to $T = 21\ ^\circ\text{C}$ during the fabrication of the sample.

Internal stresses evaluated at elevated temperature $T = 130\ ^\circ\text{C}$ (Exps. 3 and 7) shown in Fig. 9 are larger than at room temperature and extend further away from the edges. They are bi-axial compressive stress (components σ_{xx} and σ_{yy} varying along the x-line maximum $[-680\ \text{MPa}, -320\ \text{MPa}]$) and mixed tensile–compressive stress (components σ_{xx} and σ_{yy} varying along the y-line maximum $[195\ \text{MPa}, -55\ \text{MPa}]$). Since there is little difference between the results evaluated on samples S2 and S3, we can conclude that the effect of different training given to the NiTi insert on stress distribution in a virgin sample is marginal. The results reported in Figs. 8 and 9 for samples S2 and S3 can also be considered as evidence for reproducibility of the stress evaluation method.

3.2.2. Internal stress in mechanically fatigued coupons

Figs. 10 and 11 show the internal stress in the mechanically fatigued sample at room temperature (Fig. 10) and $T = 130\ ^\circ\text{C}$ (Fig. 11), respectively. Particularly noticeable is the significant increase of the magnitude of bi-axial compressive stress (components $(\sigma_{xx}, \sigma_{yy})$ along the x-line maximum $[-343\ \text{MPa}, -166\ \text{MPa}]$) compared to the virgin sample maximum $[-175\ \text{MPa}, -88\ \text{MPa}]$, Fig. 8a). On the other hand, the mechanical fatigue has negligible effect on the internal stress distribution evaluated at high temperature $T = 130\ ^\circ\text{C}$ (Fig. 11).

3.2.3. Internal stress in thermally fatigued coupons

Fig. 12 shows the internal stress distribution at temperature $T = 130\ ^\circ\text{C}$ in the sample S3 after thermal cycling between 20 °C and 100 °C (Exp. 8). There is again bi-axial compressive stress (components σ_{xx} and σ_{yy} varying along the x-line maximum $[-668\ \text{MPa}, -310\ \text{MPa}]$) and nearly uniaxial tensile stress – component σ_{xx} along the y-line maximum $[290\ \text{MPa}, 0\ \text{MPa}]$, which are almost the same values as observed in the virgin sample at $T = 130\ ^\circ\text{C}$. Unfortunately, the corresponding measurement at room temperature was not performed due to lack of time.

3.3. Internal stress evaluated through FE modeling

An alternative indirect approach to evaluate internal stress distribution in the steel coupons was adopted as follows. The internal stress distribution introduced by the NiTi insert exerting a pressure on the hole along the x-line only (no contact between the insert and coupon in the y-line) was calculated using finite element simulation (COMSOL Multiphysics).

Material parameters were taken from Table 2. Plane stress conditions were assumed and the unknown force acting on the hole edge in the x-direction was taken as a free parameter. In order to relate the actual experimental measurements with the simulations, we calculated from the FE simulated stresses the lattice strain distributions ε_{xx}, ε_{yy} along the x- and y-lines by averaging the simulated strains over gauge volume 1.6 mm × 1.6 mm around the measurement (material) point. The same diffraction elastic constants $E_{211} = 216\ \text{GPa}$, $\nu_{211} = 0.27$ were used. Thermal expansion was not considered in modeling since the strain data are already corrected for thermal expansion. Note that while doing this, the stress gradient effect on the lattice strains near the edge (second derivative of strain) is captured in the simulation but not the surface effect. Due to the little difference between lattice strains measured on samples S2 and S3 (differing by the number of compressive training cycles given to the NiTi insert), the simulated strain distributions are plotted together with the experimental data points measured on both samples S2 and S3 in Fig. 13. Using the force generated by the insert as the fitting parameter, best coincidence between the FE simulated strain distributions and experimental data points (negative position points were excluded) was obtained for forces corresponding to compressive stresses in the NiTi insert $\sigma_{\text{I}}^{20^\circ\text{C}} = -200\ \text{MPa}$ for room temperature and $\sigma_{\text{I}}^{130^\circ\text{C}} = -650\ \text{MPa}$ at high temperature. It thus appears that the increase of internal stress in the steel due to the increase of temperature from 21 °C to 130 °C corresponds to the stress increase of $\Delta\sigma_{\text{I}}^{130\text{C}-20^\circ\text{C}} = 450\ \text{MPa}$ within the insert. This corresponds to a coefficient of temperature sensitivity of transformation stress $s = \mathrm{d}\sigma_{\text{I}}/\mathrm{d}T = 4.1\ \text{MPa}\ ^\circ\text{C}^{-1}$ for the martensitic transformation in the NiTi insert. This value is slightly lower then would be expected for a virgin textured NiTi polycrystal in compression [19] but corresponds very well to what was measured in compression thermomechanical tests on trained NiTi inserts. If there are any lattice strains in the sample which are not related to the forces generated by the insert, they will not show up in the distribution of differences between the lattice strains evaluated at $T = 21\ ^\circ\text{C}$ and $T = 130\ ^\circ\text{C}$

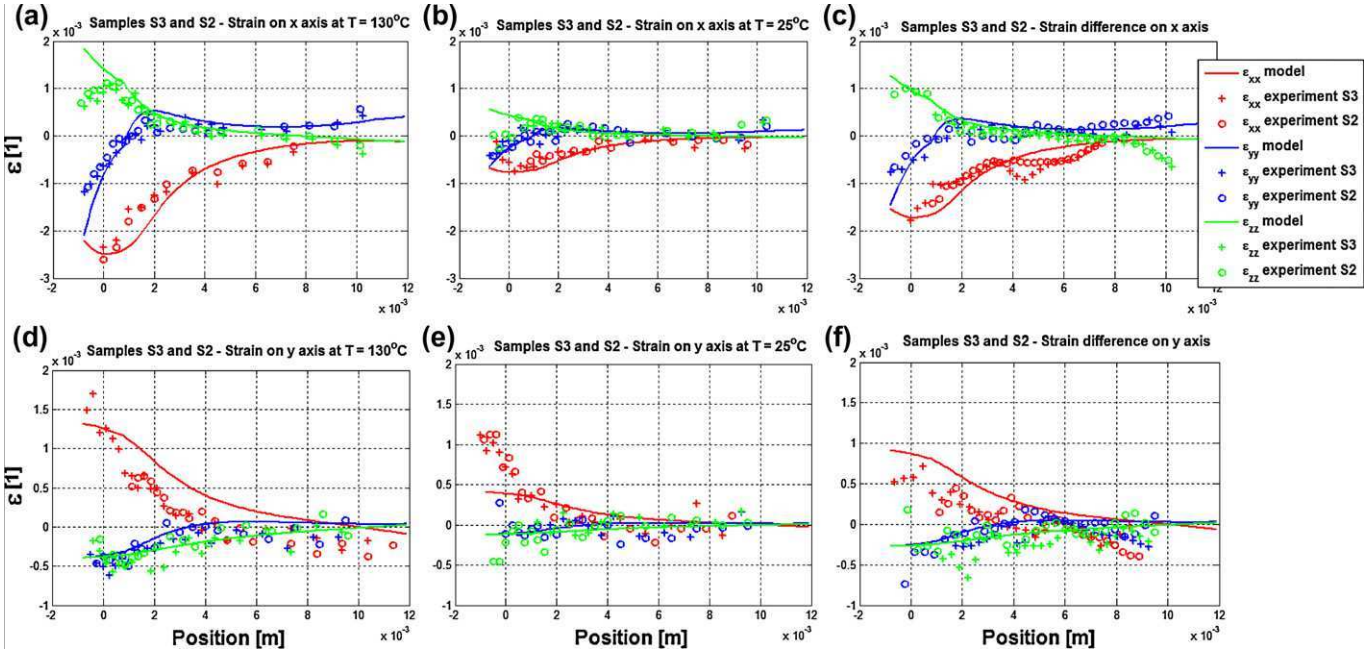

Fig. 13. Experimentally measured lattice strain distributions along the x-line (a and b) and y-line (d and e) on samples S2 and S3 plotted together with the best fit of the lattice strains from the FE simulations (average values over "gauge volume", see text) at $T = 21$ °C (b and e) and $T = 130$ °C (a and d). The figures (c and f) on the right-hand side compare the lattice strain changes caused by the raise of the temperature from 21 °C to 130 °C from experiment and simulation. Forces by which the NiTi insert acts on the steel in the x-line obtained from the fit correspond to compressive stresses $\sigma_{\mathrm{I}}^{20^\circ\mathrm{C}} = -200$ MPa at 21 °C and $\sigma_{\mathrm{I}}^{130^\circ\mathrm{C}} = -650$ MPa at 130 °C in the NiTi insert.

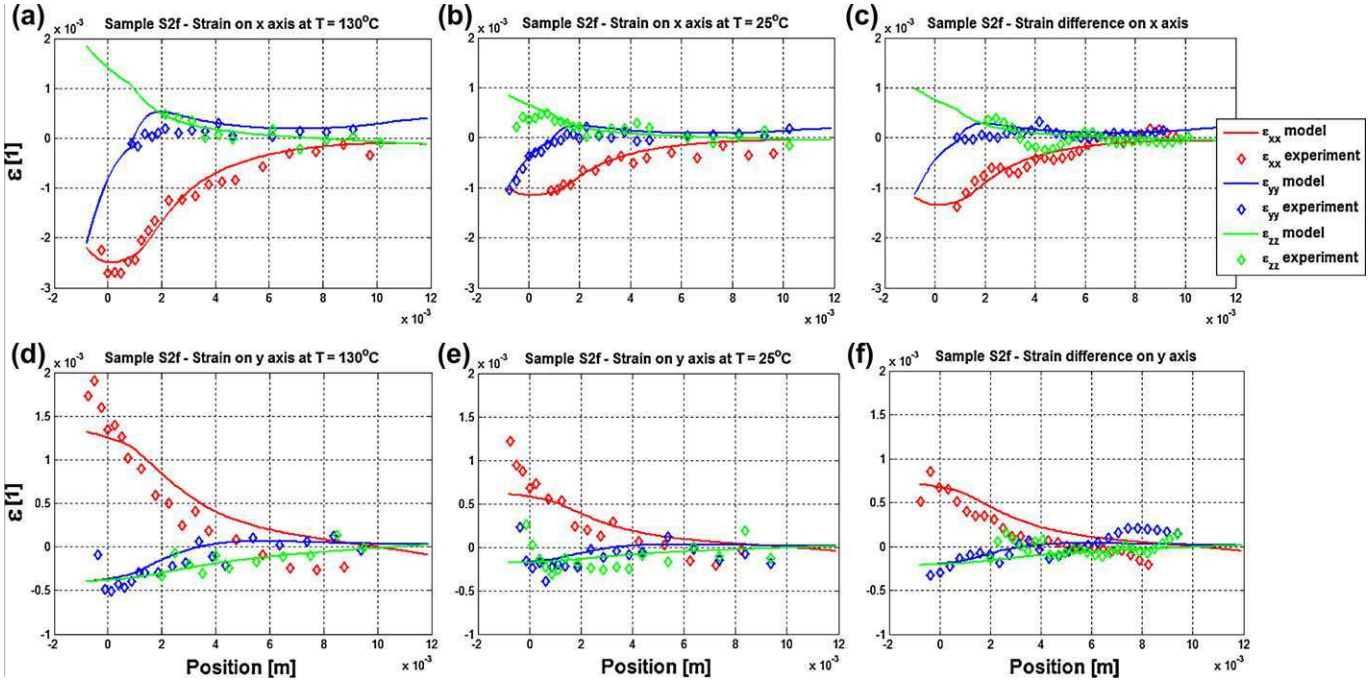

Fig. 14. Experimentally measured lattice strain distributions along the x-line (a and b) and y-line (d and e) on sample S2 subjected to mechanical fatigue plotted together with the best fit of the lattice strains from FE simulations (average values over "gauge volume", see text) at $T = 21$ °C (b and e) and $T = 130$ °C (a and d). The figures (c and f) on the right-hand side compare the lattice strain changes caused by the increase of the temperature from 21 °C to 130 °C from experiment and simulation. Forces by which the NiTi insert acts on the steel in the x-line obtained from the fit correspond to compressive stress $\sigma_{\mathrm{I}}^{20^\circ\mathrm{C}} = -300$ MPa and $\sigma_{\mathrm{I}}^{130^\circ\mathrm{C}} = -650$ MPa in the NiTi insert.

(thermal strain subtracted). Hence, we also compare differences in experimentally measured lattice strains with FE simulated differences in rightmost subfigures in Fig. 14. Since the correspondence between the fitted strain differences and experimental points is equally as good as that of the absolute strains, we can definitively conclude that

the internal stresses indeed originate from the effect of the NiTi insert expanding along the x-line with increasing temperature.

In order to evaluate the internal stress distribution in mechanically fatigued steel coupons (Figs. 10 and 11), the FE simulation was also fitted to the lattice strains measured in Exp. 5. The results are shown in Fig. 14. As a result of the fit, the forces by which the NiTi insert acts on the steel in the x-line were obtained as corresponding to the stresses in the insert $\sigma_{\mathrm{I}}^{20^{\circ}\mathrm{C}} = -300$ MPa at 21 °C and $\sigma_{\mathrm{I}}^{130^{\circ}\mathrm{C}} = -650$ MPa at 130 °C. This means that the internal stress field at room temperature changed due to mechanical cycling (from $\sigma_{\mathrm{I}}^{20^{\circ}\mathrm{C}} = -200$ MPa insert stress in the virgin coupon to $\sigma_{\mathrm{I}}^{20^{\circ}\mathrm{C}} = -300$ MPa insert stress in the fatigued coupon). The reason for this change is not completely clear yet.

4. Discussion

4.1. Internal stress field around the NiTi insert

Internal stresses appearing in steel coupon samples in the vicinity of the prestrained NiTi insert were evaluated by neutron strain scanning in our earlier work [4,5]. The steel coupon samples were, however, prepared in a different way. Since we were afraid of the stress concentration arising near the insert corners (Fig. 15) we prepared elliptical NiTi inserts and pressed them at low temperature in deformed state (~5%) into the precisely laser-cut elliptical holes. The internal stress fields evaluated from neutron strain scanning experiments performed at 24 °C, 50 °C and 70 °C at NPI Rez [5] were somewhat different from the results reported here. Directly calculated principal stress components σ_{xx}, σ_{yy}, σ_{zz} suggested compressive stress not only along the x-line and but also along the y-line, extended only ~5 mm from the insert and varied only slightly with the temperature. Strain scanning experiments were also performed on the ENGIN-X diffractometer at the ISIS facility [4] under external compressive force applied to the steel coupon along the x-line at various temperatures. The results confirmed that the residual stresses generated by the NiTi insert combine with the stress due to external force to give resultant internal stress state in the steel coupon. However, since the results reported in Refs. [4,5] were not expected, we suspected that an unsuitable technological route used to prepare the coupons could be the source of problems. The surfaces of both NiTi and steel may have been affected by rather severe laser cutting used and the elliptical inserts pressed into smaller holes probably exerted force not only along the x-direction but also in the y-direction, which was not really desired.

In order to clarify whether it is really feasible to generate the desired stress field in the steel with NiTi inserts, we performed the experiment reported here on differently manufactured steel coupon samples more suitably laser cut and containing prism-shaped and trained NiTi inserts. The main aim was to create internal stress state in the steel plate

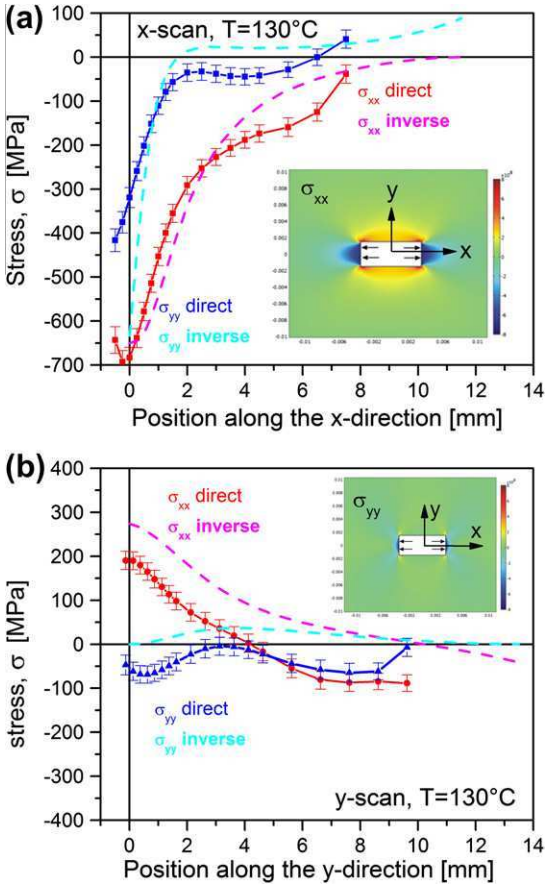

Fig. 15. Comparison of internal stresses in steel coupons around NiTi insert at $T = 130$ °C evaluated by direct calculation from measured strains and from inverse fit of FE simulations. Corresponding components of the FE simulated stress field are shown in insets.

which will significantly change with temperature between 20 °C and 130 °C in a stable and predictable manner. The results presented in Section 3 clearly prove that this has been indeed very well achieved. It was found that an internal stress field already existed in the steel at room temperature and increased with increasing temperature with a rate of 4.1 MPa °C^{-1}. The maxima of the internal stress occur near the insert edges at high temperature $T = 130$ °C (Fig. 15). These internal stresses remain below the yield stress of the steel (780 MPa) and they decrease to zero at ~7 mm away from the insert. Plastic deformation of the steel (except of the insert corners) should be theoretically avoided upon heating up to $T = \sim 160$ °C since a simple estimate suggests that the maximum internal compression stress ahead of the insert along the x-direction at 160 °C should not exceed 773 MPa ($650 + 4.1 \times 30$), which is just below the yield stress of the steel.

The mechanism is, however, relatively robust against further overheating since the compressed NiTi insert would cease to generate recovery stress when accidentally heated above ~160 °C due to its limited resistance to dislocation slip [23] giving rise to the low-temperature shape-setting (LTSS) phenomenon [18,24]. The LTSS is basically a deformation mechanism involving combination of reverse mar-

tensitic transformation and plasticity (dislocation slip and mechanical twinning) in NiTi. LTSS provides a natural limit to the maximum internal stress generated by the constrained and heated NiTi but does not destroy the ability of NiTi element to generate stress in subsequent thermal cycles [18] – i.e. the NiTi insert will continue to function properly even after it experienced overheating above 160 °C provided that the steel has not been deformed plastically during such a temperature excurse. The yield stress of the steel at high temperatures might have been locally exceeded near the insert corners where FE simulations predict significant shear stress concentrations (Fig. 15). The consequent localized plastic deformation would, however, be limited to regions around the insert corners and would have a negligible effect on the stress distribution in the regions where the strains are directly measured (Fig. 15).

On the low temperature side, since the compression stress in the NiTi insert will drop to zero at −28 °C (according to the similar estimate $-28 = 21 - 200/4.1$), the NiTi insert may become loosened at low temperatures. The stress generation mechanism thus works safely in the temperature range of about [−20 °C, 150 °C] which is, nevertheless, sufficient for a wide range of possible engineering applications. Since the stress–temperature hysteresis during fully constrained thermal cycling of prestrained NiTi is very narrow [7], the forces generated by the NiTi insert and hence the internal stress field in the steel vary almost linearly with temperature and do not depend on the cooling/heating/loading history in reasonable approximation.

One can consider the cutting disc with embedded NiTi inserts (Fig. 1) to be a prototype smart metal matrix composite consisting of structural material (steel) and engineered smart material (prestrained NiTi inserts). Smart metal matrix composites (with embedded particulate, fiber, sheet or other SMA inserts) presumably with added functionalities were already proposed a decade ago [25–29]. Armstrong and Lorentzen [29] measured thermally sensitive internal stresses (a single stress component only) within the Al matrix and NiTi fiber of thermally actuated NiTi–Al matrix composite by neutron diffraction. Murasawa and Yoneyama [30] characterized strain field around thermally actuated NiTi fibers in smart SMA polymer composite by the Digital Image Correlation method. Neither of the earlier studies, as far as we know, gave detailed quantitative information on the variation of internal stress field around the inclusion with temperature. The hereabout reported evidence on the internal stress mechanism generated by SMA inclusion can thus be considered as a proof of concept for smart metal matrix composites with embedded SMA inclusions which may facilitate their future design.

4.2. Direct vs. inverse calculation of internal stress

In order to compare the stresses evaluated by the direct and inverse methods, the internal stress distributions in a virgin sample at $T = 130$ °C obtained by both approaches are mutually compared in Fig. 15. Surprisingly, we can see that, in spite of the relatively small experimental errors associated with the direct approach and reasonably good fit of the inverse approach (Fig. 13), there are noticeable differences between the results achieved by both methods. A question of which of the calculated internal stresses are closer to the reality, thus naturally appears.

Hence let us briefly discuss principal differences between both methods. The direct calculation of stress from the piece-wise measured elastic strains using Eqs. (2), (3a), (3b), (4), (5) is the common approach widespread in the literature [8–11]. Its main advantage is that the calculated stress state originates directly from the elastic strains measured in particular measurement points. On the other hand, the point-wise assessment of stress field can easily give rise to values that do not satisfy global force balance. Considering all the possible sources of supplemental errors listed in Section 2.4 that accumulate in direct stress calculation, it may be tempting to cast doubt whether we can trust the directly evaluated stress fields.

The indirect method involving strain-fitted FE calculation is in fact similar to a kind of eigenstrain method employed recently by Korsunsky to evaluate internal stress from diffraction-evaluated internal strains [31]. This method basically searches for a permanent residual strain (eigenstrain) assumed to be the source of all measured internal elastic strains in the sample and thus source of the internal stress field of interest. Knowledge of the eigenstrain distribution is thus equivalent to the knowledge of the internal stress and strain fields in the sample. The analytical method employed to find the eigenstrain is presented in Ref. [31]. It can be formulated in the form of analytical relationships available for some specific simple cases, or generally, in the form of a numerical solution of the internal stress field within the FE framework. In the present case, the situation is simpler since we assume that we do know what the internal stress field in the steel coupon around the smart NiTi insert looks like; unknown is only the magnitude of stresses linked to a single number in the FE simulation – the magnitude of the force acting in the x-line on the hole (boundary condition). We do not employ any optimization procedure; we simply find the best fit of the FE simulated lattice strains to the set of neutron diffraction measured elastic strains (Figs. 13 and 14). The specialty of the present case is that we are mainly interested in the variation of the internal stress field with temperature. The eigenstrain is thus not permanent as considered in typical residual stress studies [31] but varies significantly with temperature, which is inherently related to the capability of the NiTi insert to generate stress upon heating [7]. Since the variation of the internal stress field with temperature must be consistent with the mechanism of its generation, the internal stress field at any temperature within the range of about [−20 °C, 150 °C] can be obtained from the FE simulation considering the linear temperature dependence of the insert stress $\mathrm{d}\sigma_{\mathrm{I}}/\mathrm{d}T = 4.1$ MPa °C^{-1}.

The indirect method also heavily relies on the precision with which the lattice strains are evaluated. Since

the internal stress field is obtained through the FE simulation, however, the balance of forces everywhere in the sample is automatically fulfilled. The impact of many of the errors listed in Section 2.4 on the resulting internal final stress field (e.g. the effect of gauge volume size, coordinate transformation, stress gradient or assumption on principal strain) is thus, compared to the direct approach, minimized. On the other hand, if the assumed eigenstrain is wrong for any reason (e.g. the actual boundary conditions are different from those assumed in the FE model), the indirect method with no optimization involved gives little chance to obtain correct internal stress field in the sample.

Based on the above brief discussion, we can now return to the differences in stress distributions obtained by both methods (Fig. 15). Due to the good agreement between the inverse FE model fitted and experimentally measured strains (Fig. 13a and b), one may deduce that the major source of the differences (Fig. 15a) is likely the multiple experimental errors on the side of the direct method. On the other hand, one can see that, for example, the inverse FE model fit of the elastic strains in the transverse scan (Fig. 13d–f) is rather poor everywhere. This might be due to the shortcomings on the side of the inverse method. Since the internal stress field must fulfill the net force balance it is not feasible to find a better fit of the complete dataset in Fig. 13. The reason could be the above-mentioned disagreement between the assumed boundary conditions (symmetry is considered in FE simulation) and reality (asymmetry due to the fact that opposite x-faces of the NiTi insert were not exactly parallel). This unaccounted disagreement will possibly become a source of supplemental error in the stress evaluation by the inverse method. It will result in non-homogeneous force distribution and/or additional shear stresses ahead of the insert. This would definitely have a drastic impact on internal stresses in the case of purely elastic inclusions (e.g. ceramics) having different CTE than steel. The superelastic NiTi insert, however, displays very large deformability compared to the steel due to stress-induced martensitic transformation (20 μm difference in NiTi insert length (~0.3% strain) is equivalent to compression stress change of only 50 MPa). The superelastic nature of the NiTi insert thus reduces the requirements for precision of the shape and placement of the insert into the hole. Hence we do not expect the imperfection in shape of the superelastic NiTi insert to be the major source of error in the present case. There must therefore be another explanation for the differences in Fig. 15 as, e.g.: (i) the residual stress in the steel plate due to its rolling texture causing the d_0 and diffraction elastic constants E_h, ν_h to be different in the x- and y-directions, or (ii) errors in the coordinate transformation (zero position setting) that may bring about asymmetry, etc.

After all, we have to admit that we do not really know where the source of the differences between the stresses evaluated by the direct and inverse method is. Both approaches have their own advantages and shortcomings. While the former approach gives more reliable information on the stress states in selected material points, the latter approach provides more reliable information on the overall internal stress field since it automatically fulfills the global force balance. It can only be concluded that, although the measurement of the relative changes of elastic strains by the neutron strain scanning method is relatively precise and evaluation of residual stress components by the direct approach has already become routine [8–11], utmost care must be taken to minimize the multiple supplemental experimental errors listed in Section 2.4 .

4.3. Fatigue of internal stress generation mechanism

The experiments (Figs. 10–12) suggest that the internal stress generation mechanism by smart NiTi insert is relatively resistant to both mechanical and thermal fatigue. This is very important since without that, practical applications cannot be seriously considered. The mechanical fatigue (Table 3, Exp. 5), nevertheless, does have an impact on the low temperature ($T = 21$ °C) internal stress field (Figs. 10, 11 and 14). The residual stress increased proportionally in magnitude after the compression fatigue cycling (fitted $\sigma_1^{20°C}$ increased from −200 MPa to −300 MPa). How can this be explained? During the compression cycling at $T = 100$ °C up to −365 MPa along the x-direction, the internal stress maxima in the steel ahead of the NiTi insert (σ_{xx} component along the x-direction) can be estimated to reach at least −527 MPa (residual stress at 100 °C). This is still well below the yield stress of the steel (780 MPa). A local compressive plastic deformation of the steel (ε_{xx}^{pl}) during compression deformation of the steel coupon with NiTi insert at 100 °C (external stress −367 MPa) was confirmed by supplemental FE simulations (not reported here) to occur mainly near the NiTi insert corners. The internal compression stress ahead of the insert ($\sigma_{xx} = -527$ MPa) monotonically decreases to $\sigma_{xx} = -367$ MPa along the x-direction and it is lowered by the action of the insert aside it (along the y-line). So the experimentally observed 100 MPa increase of the residual compressive stress after mechanical fatigue could not be rationalized by a compressive plastic deformation of the steel which would prestrain the NiTi insert even more compared to the virgin sample. Mechanical fatigue of such a smart SMA/steel composite exposed to thermomechanical service loads is currently being further investigated. There might be another possible explanation most likely related with the hysteresis and/or irreversible effects taking place in mechanically cycled NiTi insert neglected so far.

In any case, however, since the residual stress at room temperature increased after mechanical fatigue (not decreased as we were afraid of) and since it remained practically unchanged at $T = 130$ °C after mechanical or thermal fatigue, we concluded that the residual stress generation mechanism by prestrained NiTi insert is, in the first approximation, relatively fatigue-resistant.

5. Conclusions

A technology enabling deliberate introduction of internal stress fields into steel plate components by embedding superelastic NiTi shape memory alloy inserts was developed. The prestrained inserts introduce internal stresses into the surrounding steel. Since the NiTi inserts respond to temperature and stress variations differently than steel, the internal stress in such a smart composite subjected to thermomechanical service loads varies in a complex way.

In order to characterize these internal stress fields, neutron strain scanning experiments were performed on steel plate coupons with prestrained NiTi inserts at room temperature ($T = 21$ °C) and at high temperature ($T = 130$ °C). The internal stress fields were evaluated by direct calculation of principal stress components from the measured lattice strains as well as by employing an inverse strain fitted FE modeling method.

It was found that the pre-existing internal stress field in the steel at room temperature increases significantly with increasing temperature. The internal stress field is multiaxial, shows maxima of the order of -200 MPa (-650 MPa) compressive stress at temperature $T = 21$ °C ($T = 130$ °C) at the edges of the hole (insert) and decreases to zero ~5–7 mm away from it. Variation of the internal stress field with temperature is approximately linear nonhysteretic (stress rate ~4.1 MPa °C^{-1}) and reproducible. It is estimated that this mechanism of internal stress generation can be safely applied in the temperature range from -20 °C to 150 °C.

By performing additional experiments also on fatigued coupons, it was found that the mechanism is fairly resistant to thermal as well as mechanical fatigue. The predictability of internal stress fields and fatigue endurance of the mechanism are promising for further development of engineering applications of smart metal matrix composites with embedded SMA inclusions.

Acknowledgements

The authors acknowledge the support from Czech ILL Access Project INGO LA 339 as well as the kind assistance of the ILL staff (Thilo Pirling and Jean-Claude Collet-Fenetrier). Also acknowledged is the support through Czech National Research Projects No. P108/10/1296, 106/09/1573 and Institutional Projects AV0Z10100520 and AV0Z20760514.

References

[1] Withers PJ, Bhadeshia HKDH. Mater Sci Technol 2001;17:355.
[2] Withers PJ, Bhadeshia HKDH. Mater Sci Technol 2001;17:366.
[3] Venter AM, La Grange CP, Hofmann F, Jun TS, Belnoue J, van Heerden PR, et al. Z Kristallogr 2009;30(Suppl.):315.
[4] Malard B, Šittner P, Pilch J, Davydov V, Oliver EC. Stress distributions around active NiTi inserts in smart cutting discs. In highlight – ISIS annual report; 2008.
[5] Davydov V, Lukáš P, Vrána M, Malard B, Maximov V, Pilch J, et al. Mater Sci Eng A 2010;527:3310.
[6] FP6 collective research project for SMEs/PROSTONE/, COLL-CT-2005-516417.
[7] Šittner P, Vokoun D, Dayananda GN, Stalmans R. Mat Sci Eng A 2000;286:298.
[8] Lorentzen T, Leffers T. In: Hutchings TB, Krawitz AD, editors. Measurement of residual and applied stress using neutron diffraction. NATO ASI series E applied science. Alphen aan den Rijn: Kluwer Academic Publishers; 1992. p. 253.
[9] Withers PJ. CR Phys 2007;8:806.
[10] Webster GA, Wimpory RC. J Mater Process Technol 2001;117:395.
[11] Hutchings MT, Withers PJ, Holden TM, Lorentzen T. Introduction to the characterization of residual stress by neutron diffraction. Boca Raton (FL): CRC Press; 2005.
[12] Taylor JR. An introduction to error analysis. 2nd ed. Sausalito: University Science Books; 1997.
[13] Pirling T, Bruno G, Withers PJ. Mater Sci Eng A 2006;437:139.
[14] Santisteban JR, Daymond MR, James JA, Edwards LJ. Appl Cryst 2006;39:812.
[15] Bourke MAM, Dunand DC, Ustundag E. Appl Phys A: Mater Sci Proc 2002;74:1707.
[16] Harjo S, Ito T, Aizawa K, Arima H, Abe J, Moriai A, et al. Mater Sci Forum 2011;681:443.
[17] Wang XL, Holden TM, Rennich GQ, Stoica AD, Liaw PK, Choo H, et al. Phys B: Condens Matter 2006;67:385–6.
[18] Šittner P, Pilch J, Heller L, Malard B, Delville R, Curfs C. Low temperature shape setting of NiTi wires and textiles for medical devices, presented at SMST 2011. J Mech Eng Perform, in press.
[19] Šittner P, Lukáš P, Novák V, Daymond MR, Swallowe GM. Mater Sci Eng A 2004;378:97.
[20] Daymond MR, Priesmeyer HG. Acta Mater 2002;50:1613.
[21] <http://www.engineeringtoolbox.com/linear-expansion-coefficients-d_95>.
[22] Pirling T. Proc Eng 2011;10:2147.
[23] Delville R, Malard B, Pilch J, Sittner P, Schryvers D. Int J Plast 2011;27:282.
[24] Pilch J, Sittner P, Heller L, Delville R, in: SMST 2010-extended abstracts. ASM Int; 2010.
[25] Furuya Y, Sasaki A, Taya M. Mater Trans JIM 1993;34:333.
[26] Wei ZG, Tang CY, Lee WB. J. Mater Process Technol 1997;69:68.
[27] Porter GA, Liaw PK, Tiegs TN, Wu KH. JOM 2000;52:52.
[28] Wei ZG, Sandstrom R, Miyazaki S. J Mater Sci 1998;33:3763.
[29] Armstrong WD, Lorentzen T. Metal Mater Trans A 2002;33:3535.
[30] Murasawa G, Yoneyama S. Mater Trans JIM 2006;47:766.
[31] Korsunsky AM. J Strain Anal Eng Des 2009;44:29.